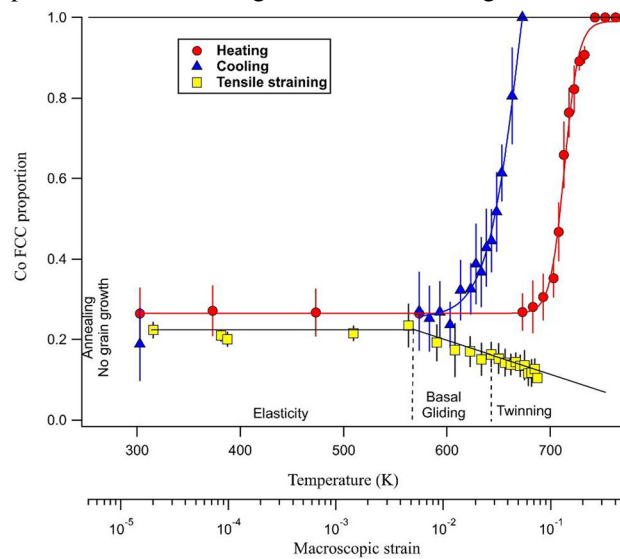


Experimental Investigation of Allotropic Transformation of Cobalt: Influence of Temperature Cycle, Mechanical Loading and Starting Microstructure



NADJIB ISKOUNEN, PIERRE-ANTOINE DUBOS, JAMAL FAJOU, MICHEL CORET, MARIE-JOSÉ MOYA, BAPTISTE GIRAULT, NICOLAS BARRIER, NICOLAS BRUZY, ERIC HUG, and DAVID GLOAGUEN

The allotropic phase transformation in polycrystalline high-purity cobalt is incompletely reversible and exhibits a temperature hysteresis. This leads to the presence of a FCC metastable phase at room temperature, which alters the mechanical properties. Moreover, this phase transformation seems to be induced by the plastic deformation. The influence of thermal cycling and initial microstructure on the phase transformation has been analyzed with different experimental approaches, namely *in situ* x-ray diffraction, differential scanning calorimetry and high-temperature digital image correlation analysis. A multiscale analysis, under an *in situ* tensile test, has been adopted to follow the phase transformation induced by the plastic deformation. The main result shows that the transformation is initiated by basal slip mechanisms, in competition with twinning mechanisms during the second work-hardening stage.



<https://doi.org/10.1007/s11661-021-06142-7>

© The Minerals, Metals & Materials Society and ASM International 2021

NADJIB ISKOUNEN, PIERRE-ANTOINE DUBOS, JAMAL FAJOU, MICHEL CORET, MARIE-JOSÉ MOYA, BAPTISTE GIRAULT, NICOLAS BRUZY, and David GLOAGUEN are with the Université de Nantes - Centrale Nantes, Institut de Recherche en Génie Civil et Mécanique (UMR CNRS 6183), 58 rue Michel Ange - BP 420, 44606 Saint-Nazaire Cedex, France. Contact e-mail: pierre-antoine.dubos@univ-nantes.fr. NICOLAS BARRIER and ERIC HUG are with the UNICAEN, Laboratoire de Cristallographie et Sciences des Matériaux (UMR CNRS 6508), 6 boulevard Maréchal Juin, 14050 Caen, France.

Manuscript submitted August 20, 2020; accepted December 21, 2020.

Article published online February 24, 2021

I. INTRODUCTION

MECHANICAL properties of metallic materials, such as high-purity cobalt, are directly linked to crystallographic phase structures and microstructure defect presence. The mechanical behavior of two-phase cobalt remains unclear when the phase distribution and evolution are not controlled. Results of the literature

exhibited an important improvement of the mechanical properties of cobalt when it presents a two-phase structure.^[1]

High-purity polycrystalline cobalt exhibits an allotropic transformation (reversible and diffusionless) from HCP (hexagonal close-packed) phase to FCC (face centered-cubic) on around 713 K (austenitic transformation). The reverse transformation, from FCC to HCP phase (named martensitic transformation^[2–4]), occurs roughly at 603 K. The cobalt transformations lead to a temperature hysteresis that depends on the number of applied thermal cycles.^[4,5]

Usually, cobalt martensitic transformation remains incomplete. Consequently, a residual FCC phase persists at room temperature in association with the predominant HCP phase.^[3,6,7]

Sanderson^[7] investigated the tensile properties of polycrystalline cobalt at room temperature to obtain a stable HCP phase using different initial retained FCC phase volume proportions, grain sizes and purity samples. He found that the retained FCC phase volume fraction of polycrystalline cobalt at room temperature depends on the thermal history, purity and grain size. Using x-ray diffraction (XRD), Marx *et al.*^[8] studied the strain-induced phase transformation, at room temperature in a 2- μm -thick film deposited on a polyimide substrate using *in situ* tensile tests. They showed that the untransformed metastable FCC phase was reduced from 51 to 8 pct when the total macroscopic strain increased from 2 up to 8 pct.

Martinez *et al.*^[9] investigated the dislocation microstructure of deformed polycrystalline cobalt by analyzing the different modes responsible for plastic strain. They observed two distinct work-hardening stages: stage A, up to 4 pct of plastic strain, where basal dislocation glide is the main deformation mechanism; stage B, where plastic deformation is mostly accommodated by twinning mechanisms, in agreement with Seeger *et al.*^[10] These different deformation stages were also observed by Fleurier *et al.*^[11]

HCP cold-rolled metals tend to exhibit a specific deformation texture, called basal texture. A principal $\{00.1\}$ basal texture component was indeed observed in polycrystalline rolled cobalt by electron backscatter diffraction (EBSD).^[3,9] The phase transformation in high-purity cobalt occurs by the glide of dislocations due to the shear stress on the habit $\{111\}_{\text{FCC}}//\{00.1\}_{\text{HCP}}$ planes.^[12] Hesemann *et al.*^[13,14] studied the influence of the texture on martensitic transformation in cobalt thin films by varying the habit plane inclination angle from the film surface at different temperatures using *in situ* synchrotron XRD. They observed that the phase transformation depends on the inclination angle between the $\{111\}_{\text{FCC}}//\{00.1\}_{\text{HCP}}$ planes and the film surface, this transformation arising more easily at an intermediary inclination of about 20 deg.

The present study focuses on the understanding of the allotropic transformation of polycrystalline high-purity cobalt, which might be affected by the initial microstructure as well as the thermal and mechanical loadings, using several characterization techniques. After a detailed description of the experimental methods, the

allotropic transformation behavior during the thermal cycle, such as the evolution of the FCC phase volume proportion using the *in situ* XRD laboratory technique, is presented. Moreover, the influence of the number of applied thermal cycles on the energetic parameters, carried out by differential scanning calorimetry (DSC), is reported. In addition, an overview of the effect of the initial microstructure (modulated by various annealing treatments) on the phase transformation is given. Finally, the strain effect on the phase transformation at room temperature is presented. *In situ* tensile tests under XRD were used to study the influence of the strain hardening mechanisms on the phase transformations.

II. MATERIALS AND METHODS

A. Characterization of As-Received Material

Commercial polycrystalline cobalt sheets (Goodfellow Company) of high-purity (99.9 wt pct), cold-rolled to 0.5 mm thickness and in a recrystallized state, were used for the present study.

Metallographic examinations of the as-received material revealed that the average grain size is about 24 μm , with a standard deviation of 12 μm . The initial microstructure displays two sets of grain shapes corresponding to the two phases (HCP and FCC). Figure 1 shows a predominant polygonal grain family population corresponding to the HCP phase and a limited number of triangular and plate geometries for the FCC phase.

The initial crystallographic textures and retained FCC phase ratio at room temperature were determined using the XRD technique. A four-circle Seifert XRD3003 PTS diffractometer equipped with a Euler cradle, position-sensitive detector (PSD) with a 2θ effective window of 8.6 deg, 1-mm-diameter collimator and IDS camera (to align the sample in the center of the goniometer) was used. A Cr anode ($\text{CrK}_{\alpha 1+2}$ radiation), operating at 30 kV and 35 mA, was used (wavelength $\lambda = 2.28964 \text{ \AA}$). The K_{β} component of the Cr radiation was eliminated using a vanadium filter installed in front of the detector.

Using the θ - 2θ scanning mode, the diffraction spectra were recorded from 60 deg to 106 deg in 2θ with a step size of 0.05 deg and a counting time of 126 s/step. The analyzed reflections are listed in Table I. The initial averaged FCC phase volume proportion, obtained according to the method described in Section II-D-3, is about 22 pct.

The crystallographic textures were determined from the orientation distribution functions (ODF) calculated by the WIMV method implemented in the BEARTEX software^[15] and were obtained from experimental pole figures (PFs) $\{10.0\}_{\text{HCP}}$, $\{00.2\}_{\text{HCP}}$, $\{10.1\}_{\text{HCP}}$, $\{10.2\}_{\text{HCP}}$, $\{111\}_{\text{FCC}}$ and $\{200\}_{\text{FCC}}$ with average error coefficients in the order of 0.08, except for the initial FCC phase (0.2). The declination (ψ) and azimuthal (φ) angles varied from 0 to 65 deg ($\Delta\psi = 5 \text{ deg}$) and from 0 to 355 deg ($\Delta\varphi = 5 \text{ deg}$), respectively. At $\varphi = 0 \text{ deg}$ and $\psi = 90 \text{ deg}$, the scattering vector was aligned with the rolling direction (RD).

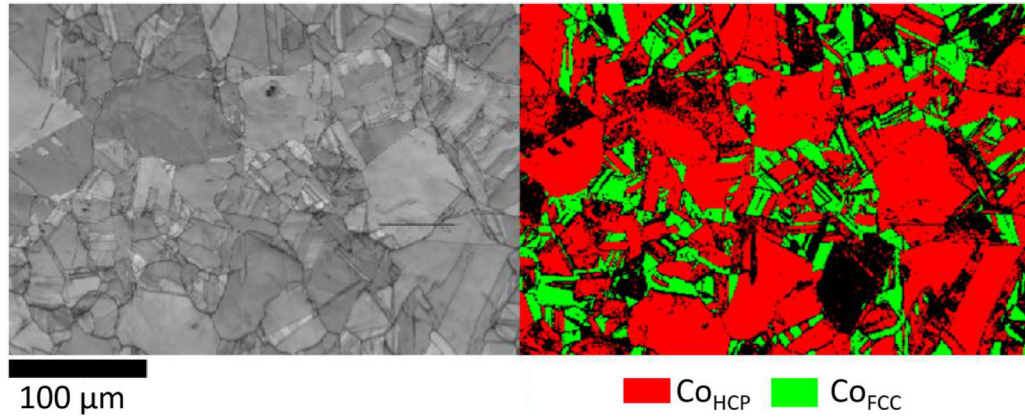


Fig. 1—EBSD image quality (IQ) map and phase cartography of the as-received cobalt microstructure.

Table I. XRD Reflections Tracked for Each Experiment and the Plane Family Couples Used for the Phase Volume Fraction Calculations

	Studies		
	Strain Influence on Phase Transformation	Texture Analysis	Thermal Cycle Influence on Phase Transformation
HCP plane families	{10.0}, {00.2}, {10.1} and {10.2}		{10.0}, {00.2}, {10.1}, {10.3} and {10.2}
FCC plane families	{111} and {200}		
Planes family couples	$\{10.0\}_{\text{HCP}}/\{111\}_{\text{FCC}}$, $\{10.0\}_{\text{HCP}}/\{200\}_{\text{FCC}}$, $\{00.2\}_{\text{HCP}}/\{111\}_{\text{FCC}}$, $\{00.2\}_{\text{HCP}}/\{200\}_{\text{FCC}}$, $\{10.1\}_{\text{HCP}}/\{111\}_{\text{FCC}}$, $\{10.1\}_{\text{HCP}}/\{200\}_{\text{FCC}}$, $\{10.2\}_{\text{HCP}}/\{111\}_{\text{FCC}}$, $\{10.2\}_{\text{HCP}}/\{200\}_{\text{FCC}}$		$\{10.0\}_{\text{HCP}}/\{111\}_{\text{FCC}}$, $\{10.0\}_{\text{HCP}}/\{200\}_{\text{FCC}}$, $\{00.2\}_{\text{HCP}}/\{111\}_{\text{FCC}}$, $\{00.2\}_{\text{HCP}}/\{200\}_{\text{FCC}}$, $\{10.1\}_{\text{HCP}}/\{111\}_{\text{FCC}}$, $\{10.1\}_{\text{HCP}}/\{200\}_{\text{FCC}}$, $\{10.3\}_{\text{HCP}}/\{111\}_{\text{FCC}}$, $\{10.3\}_{\text{HCP}}/\{200\}_{\text{FCC}}$, $\{10.2\}_{\text{HCP}}/\{111\}_{\text{FCC}}$, $\{10.2\}_{\text{HCP}}/\{200\}_{\text{FCC}}$

B. Thermal Cycles and Differential Scanning Calorimetry

The influence of the initial microstructure (grain size and retained FCC proportion) on the phase transformation was studied using DSC. First, cobalt samples were annealed at a temperature set between 573 K and 1273 K for 1 hour, and cooled down with a cooling rate of 40 K/min. In a second step, DSC scanning was performed on four samples (as-received and annealed at 573, 673 and 773 K) with a heating path up to 773 K and then down to 593 K (heating and cooling rate = 10 K/min) according to the methodology described by Ray and Smith^[2] to measure the HCP → FCC and FCC → HCP transformation temperatures. Ray and Smith^[2] showed that the austenitic transformation temperature increases with higher heating rates. A phase quantification was carried out at 743 K with the same selected rate to ensure that the transformation was complete.

C. Macroscopic Dilatometric Test

Dilatometric tests were performed using a homemade device on dog bone-shaped tensile specimens.^[16,17] The

samples were machined by electroerosion along the rolling direction. The gage section has 5 mm length, 5 mm width and 0.5 mm thickness. The sample is placed into a testing box under low argon pressure and heated by the Joule effect. A two-color pyrometer (SensorTherm METIS M322) measures the temperature at the center of the specimen starting from 300°C because of its intrinsic emissivity. Based on an alumina-based paint, a speckle pattern is deposited on the surface of the sample with a fine nozzle airbrush. During the test, a high-resolution camera (Prosilica GT6600: 6576 × 4384 px²) records images of a 9 × 6 mm² area. The macroscopic total strain field is then computed using the digital image correlation method (VIC software). The images and temperature values are recorded simultaneously to establish the dilatometric curve (total strain versus temperature).

D. In Situ X-Ray Diffraction Measurements

1. Temperature

In situ experiments were carried out to study the influence of temperature on the phase transformation

Table II. Applied Temperatures for *In Situ* XRD Experiments During the Thermal Cycle (Heating Rate 0.5 K/s Between Each Temperature Step—1 h Acquisition Duration for Each Temperature)

	Temperature Range (K)	Temperature Step (K)
Initial	at 303	—
Heating	from 373 to 673	100
	from 673 to 703	10
	from 703 to 733	5
	from 733 to 773	10
Cooling	from 773 to 673	100
	from 673 to 653	10
	from 653 to 623	5
	from 623 to 573	10
Final	at 303	—

behavior. The variation of the phase (FCC and HCP) ratio during heating and cooling was evaluated by XRD technique on a Bruker D8 advance diffractometer operating at 40 kV and 40 mA equipped with a primary germanium (111) Johansson monochromator ($\lambda_{K_{\alpha 1}} = 1.5406 \text{ \AA}$) and a Lynxeye detector. The XRD patterns were recorded in the 2θ angular range 35 to 95 deg with a step size of 0.015 deg and a counting time of 0.9 s/step. The thermal cycle (with a rate of 0.5 K/s) was conducted between 303 and 773 K. Despite the short counting time, the signal-to-noise ratios are only slightly affected, and the quality of the fitting shows, on average over all the peaks, an error of 0.0011 deg for the position and < 5 pct for the integrated intensities. The listed diffraction peaks presented in Table I were monitored for each temperature of the thermal cycle described in Table II. The temperature ranges and heating step were chosen around the temperatures of austenitic and martensitic transformations.

2. Tensile tests

In situ uniaxial monotonic tensile tests were carried out at room temperature to study the influence of elastoplastic strain on the allotropic transformation. These mechanical tests were performed on a DEBEN device equipped with a load cell of 5 kN capacity and controlled by the displacement between clamping jaws. The dog bone-shaped tensile specimens were machined by electroerosion with a gage section of 26 mm length, 7 mm width and 0.5 mm thickness. In the same way, as explained in 2.3, the samples were also speckled and images were recorded during the test. Digital image correlation was then processed to obtain the macroscopic total strain fields.

The samples were strained stepwise up to 7.8 pct with a strain rate of 0.2 mm/min. At each straining step, and after a stress relaxation of about 20 minutes to obtain stable mechanical fields over the entire diffracting volume, the camera images were captured and the 2θ diffraction spectra were analyzed with an angle ranging from 60 to 106 deg with a step size of 0.05 deg and counting time of 126 s/step. The reflections listed in Table I were analyzed. The crystallographic texture was also determined after the *in situ* tensile experiment as described in 2.1.

3. Analysis method

Experimental XRD peak profiles were fitted by a pseudo-Voigt function, which takes into account the $K_{\alpha 1}$ - $K_{\alpha 2}$ doublet.^[18] For each diffraction peak, the background was fitted through a second-order polynomial function. Before peak profile analysis, angular corrections (Lorentz, polarization and absorption factors) are also applied.^[19]

The FCC phase volume fraction (denoted f^{FCC}) was determined for each measurement point using Eq. [1] as formulated by Bonarski *et al.*^[20]:

$$f^{FCC} = \left(1 + \frac{I_{hkl}^{HCP} R_{hkl}^{FCC}}{I_{hkl}^{FCC} R_{hkl}^{HCP}} \right)^{-1} \quad [1]$$

where I_{hkl} is the integrated intensity of the corresponding $\{hkl\}$ peak. R_{hkl} is the reflectivity of the lattice plane $\{hkl\}$ and is given by the following Eq. [2] introduced in the literature^[20]:

$$R_{hkl} = \frac{1}{v^2} |F_{hkl}|^2 \left(\frac{1 + \cos^2(2\theta)}{\sin^2(2\theta) \cos(\theta)} \right) m \frac{e^{-2M}}{\mu} \quad [2]$$

where v is the volume of the unit cell (in \AA^3), F_{hkl} is the structure factor, 2θ is the considered Bragg angle (in rad), m is the $\{hkl\}$ planes multiplicity factor, μ is the linear absorption coefficient (in cm^{-1}), and e^{-2M} is the Debye-Waller factor.^[21,22]

The volume fraction of the phases was calculated from several groups of family planes, as presented in Table I, to obtain the average FCC phase distribution and evaluate the influence of the texture on the quantitative phase analysis.

III. RESULTS AND DISCUSSION

A. Allotropic Transformation Characterization During the Thermal Cycle

1. Phase proportion evolution and typical temperatures

To characterize the HCP \leftrightarrow FCC transformation behavior, the evolution of the integrated diffraction peak intensity for each reflection corresponding to the HCP and FCC phases was recorded as a function of the temperature. An example is given in Figure 2 for $\{111\}_{FCC}$ and $\{00.2\}_{HCP}$ reflections during heating and cooling. The volume fraction of the phases can be determined according to Eqs. [1] and [2].

Figure 3 gives the FCC phase proportion evolution during the thermal cycle described in Table II. During heating, the HCP \rightarrow FCC transformation begins at the austenitic start temperature denoted $A_s = 673 \text{ K}$ and ends at the austenitic finish temperature named $A_f = 743 \text{ K}$. During cooling, the reverse transformation FCC \rightarrow HCP arises at the martensitic start temperature $M_s = 673 \text{ K}$ and comes back to its original state when the martensitic finish temperature of $M_f = 593 \text{ K}$ is reached. The two experimental curves can be fitted by sigmoidal laws, which allow defining the transformation temperatures $T_{HCP-FCC}$ and $T_{FCC-HCP}$. These temperatures are determined when the FCC

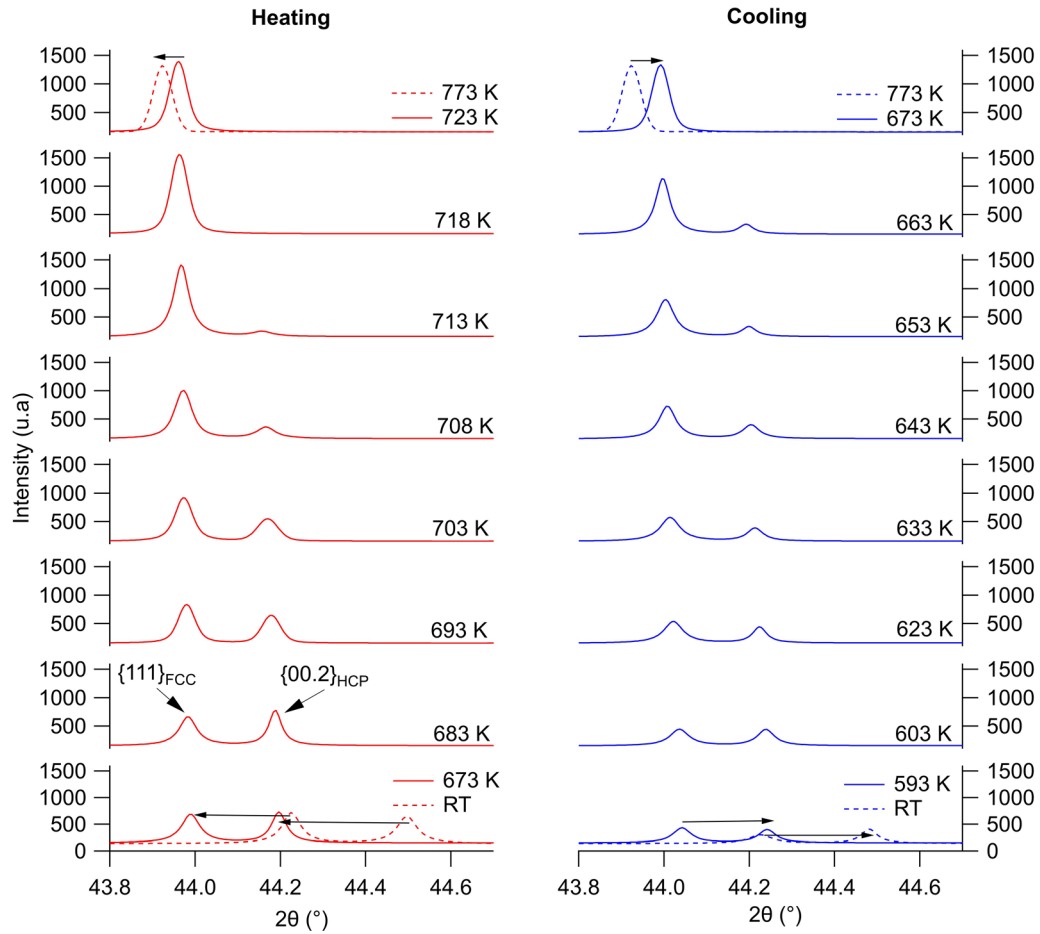


Fig. 2—Diffraction patterns for $\{111\}_{\text{FCC}}$ and $\{00.2\}_{\text{HCP}}$ reflections during heating and cooling.

proportion has a relative variation of 50 pct over the temperature cycle, knowing that the initial proportion is 26 pct and that the transformation is complete during heating. With this methodology, $T_{\text{HCP-FCC}} = 714$ K and $T_{\text{FCC-HCP}} = 653$ K are obtained, revealing a temperature hysteresis around 60 K. The diffraction patterns also enabled identifying CoO and Co_3O_4 oxide formation from 673 K, which persists when cooling down to room temperature. It is important to point out that the presence of a thin oxide layer does not affect the quantification of the HCP and FCC phase proportions. Finally, it seems that the phase transformation is faster during heating than during cooling. This can be related to the phase transformation mechanism, which is based on dislocation movements,^[23] themselves favored by an increase in temperature.

2. Lattice strain measurements during the thermal cycle

Lattice strain of each $\{hkl\}$ plane family can be determined considering the lattice spacing (d_{hkl}) as an elastic strain gage using the following equation^[24]:

$$\varepsilon\langle(hkl)\rangle_{V_d} = \ln\left(\frac{\langle d_{hkl} \rangle_{V_d}}{d_0^{hkl}}\right) = \ln\left(\frac{\sin\theta_0(hkl)}{\langle \sin\theta(hkl) \rangle_{V_d}}\right) \quad [3]$$

$\langle \varepsilon(hkl) \rangle_{V_d}$ is the elastic lattice strain. $\langle \rangle_{V_d}$ indicates an averaging over diffracting grains for the considered $\{hkl\}$ reflection. For a given $\{hkl\}$ reflection, d_0^{hkl} and $\theta_0(hkl)$ are the interplanar spacing and the diffraction angle (Bragg angle), respectively, in the undeformed sample, *i.e.*, prior to any thermal or mechanical loading. Figure 4(a) gives the evolution of the lattice strains observed for different $\{hkl\}$ reflection of the two phases during the applied thermal cycle. This evolution is linear for both heating and cooling, enabling estimation of the coefficients of thermal expansion (CTE) α_{hkl} for each plane family within the analyzed polycrystal. The obtained values are represented in Figure 4(b) and are in agreement with the literature.^[21] Matsumoto^[4] also showed that the CTE of HCP single crystals is substantially affected by the orientation of the c -axis within the sample coordinate system. The thermal cycle induces a large strain; the largest one actually reaches $> 8000 \mu$ strain ($\times 10^{-6}$ mm/mm) for the $\{00.2\}_{\text{HCP}}$ set of grains. The main thermal dilatation occurs then along the $[00.2]_{\text{HCP}}$ direction. During cooling, plastic deformations are induced and can be explained by the presence of residual lattice strains. These results agree with prior investigations on high-purity cobalt showing slipping lines due to plastic deformation during the thermal cycle.^[23,25]

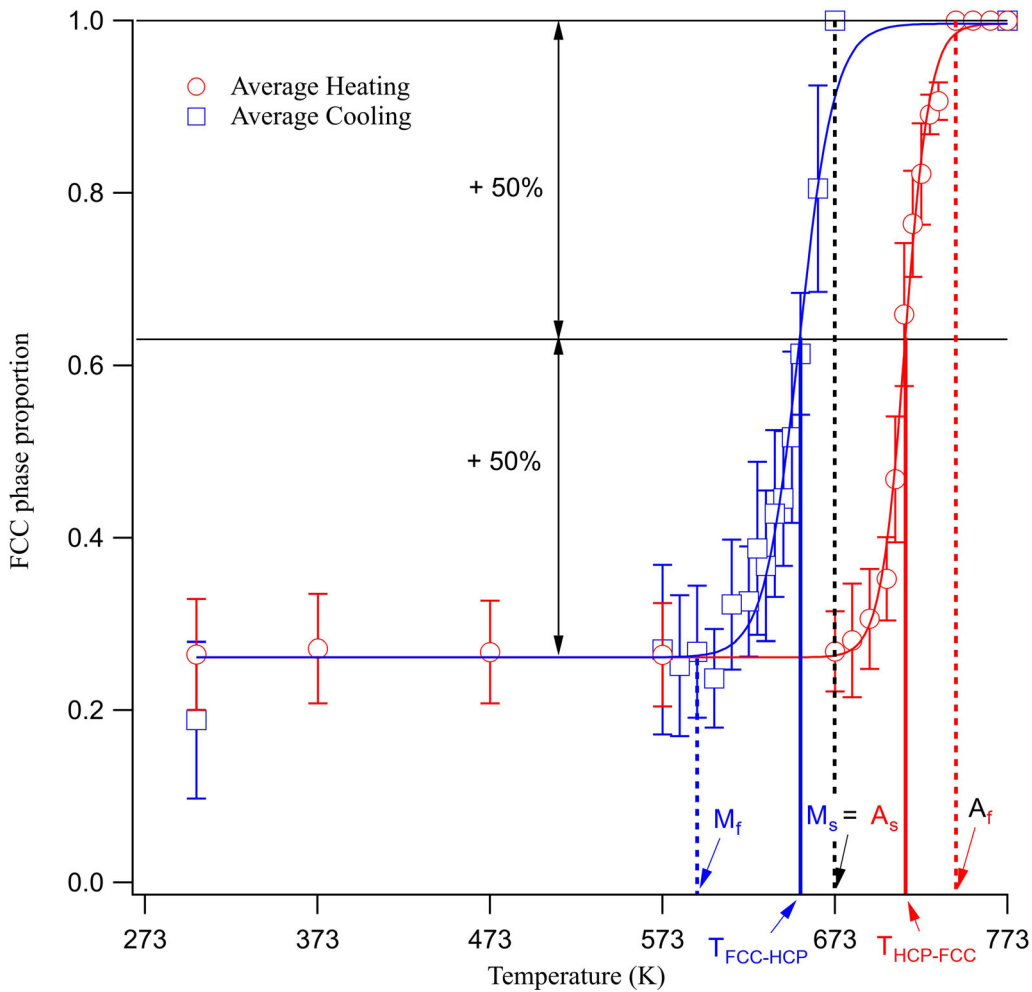


Fig. 3—Volume fraction of FCC phase during heating (red circle) and cooling (blue square) of cobalt calculated from the XRD data. Error bars are the standard deviation on the eight couples of family planes (Color figure online).

Figure 4(c) shows the residual lattice strains present after the thermal cycle for each analyzed reflection. Initially, residual strains can be considered negligible because of the annealed character of the as-received materials. This allows considering the initial state of samples as a strain-free reference. After the thermal cycle, residual lattice strains slightly increased, especially for $\{00.2\}_{\text{HCP}}$, $\{10.2\}_{\text{HCP}}$ and $\{200\}_{\text{FCC}}$ reflections. Regarding uncertainties, only the $\{00.2\}_{\text{HCP}}$ planes present an unambiguous residual strain of a few hundred μ -strains in tension. As shown in Figure 4, these residual strains measured after a thermal cycle are related to the phase transformation and its associated volume variation as well as the accommodation related to the thermal and plastic anisotropies.

3. Macroscopic thermal dilatation

The post-treatment of image correlation results enables access to the ε_{xx} (parallel to RD), ε_{yy} (parallel to the transverse direction (TD)) and γ_{xy} strain components. Figure 5 shows the dilatometric curves obtained by coupling the temperatures measured by the pyrometer (at the center of the sample) and the strain fields obtained

by the image correlation method. The phase transformation induces a change of volume due to the change of lattice structures of about 0.3 pct in the case of high-purity polycrystalline cobalt, as reported in the literature.^[12,25,26] Hence, in the temperature range between 573 K and 773 K, the dilatometric curve is the consequence of the competition between thermal expansion and volumetric change. As can be seen, both dilatometric curves along x and y display a temperature hysteresis caused by the phase transformation, which is not observed on the lattice strains during the thermal cycle (see Figure 4(a)). The difference in the scale of analysis may be the reason for these observations. XRD results exhibit the combination of macroscopic (or Type I) and intergranular strains (or Type II) whereas dilatometry only gives access to macroscopic strains. The hysteresis of the ε_{xx} dilatometric curve is qualitatively slightly broader than that of the ε_{yy} dilatometric curve and could be explained by a slight anisotropy or texture effect. Moreover, hysteresis occurs systematically between the temperatures $M_f = 593$ K and $A_f = 743$ K. Beyond the austenitic finish temperature, A_f , the dilatometric curve displays a linear evolution (for both of ε_{xx} and ε_{yy}) with

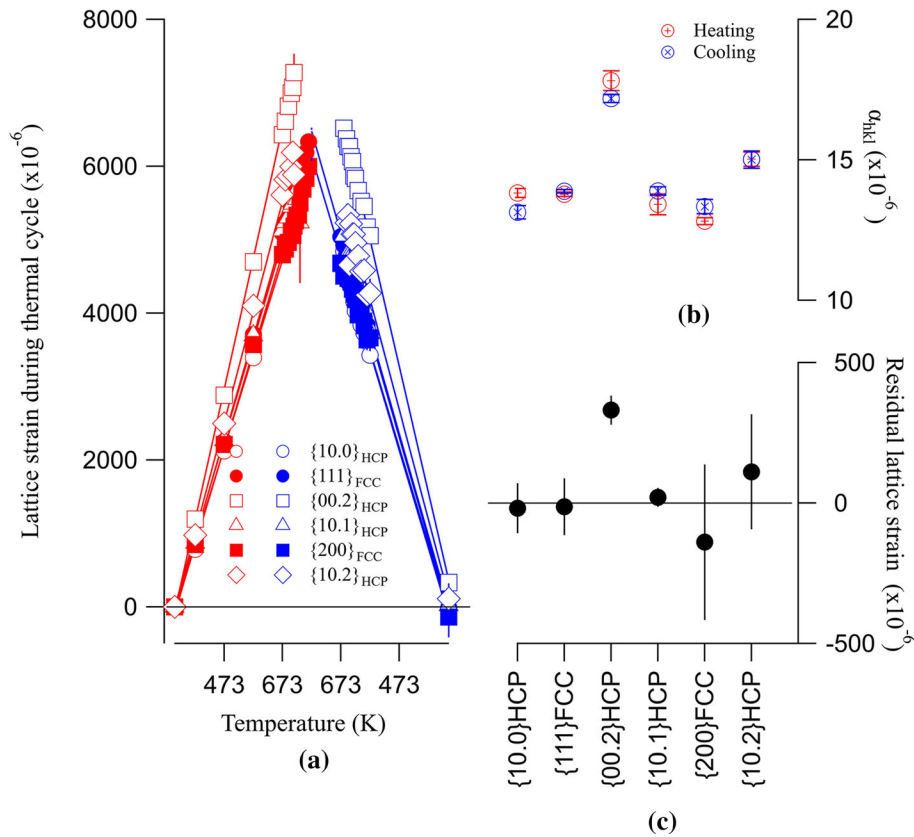


Fig. 4—Mechanical state during the thermal cycle considering the different tracked plane families. (a) Lattice strain evolution during heating (red) and cooling (blue). (b) Thermal expansion coefficients during heating (red open circle) and cooling (blue open circle) obtained from XRD results. (c) Measured residual lattice strains after (black solid circle) the thermal cycle (Color figure online).

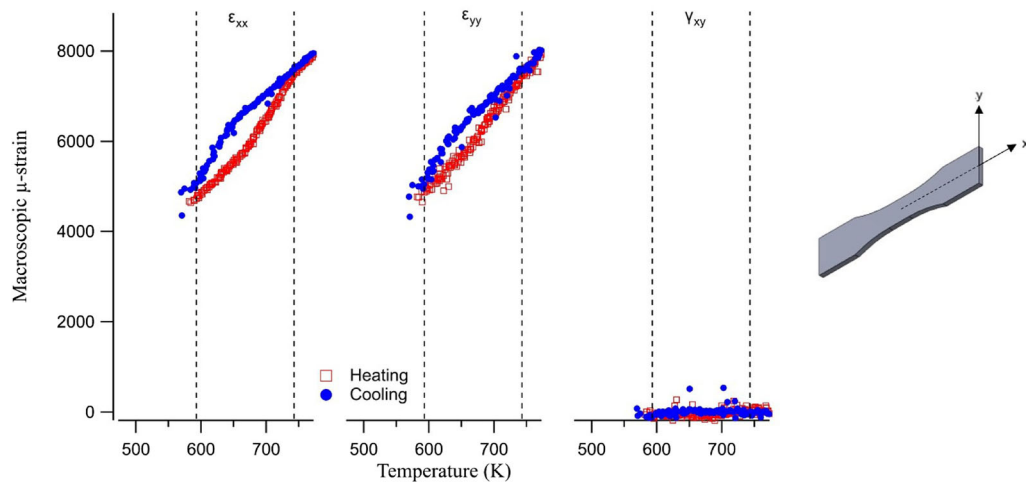


Fig. 5—Dilatometric curves according to ϵ_{xx} , ϵ_{yy} and γ_{xy} during the thermal cycle (for this experiment x corresponds to the rolling direction).

temperature that matches a pure thermal expansion or contraction during heating or cooling, respectively. ϵ_{xx} and ϵ_{yy} strain components exhibit a quasi-equibiaxial strain state with an order of magnitude similar to the measured lattice strains induced by the thermal cycle (see Figure 4). Finally, the dilatometric curve of γ_{xy} clearly highlights the absence of macroscopic planar shearing during the thermal cycle.

4. Influence of initial microstructure on the allotropic transformation

Figure 6 shows the influence of annealing temperature on the grain size and on the volume fraction of the retained FCC phase. In the present work, an annealing duration of 1 hour was chosen to have a limited granular growth so that grain size evolution remained a minor contribution to the microstructure changes no matter

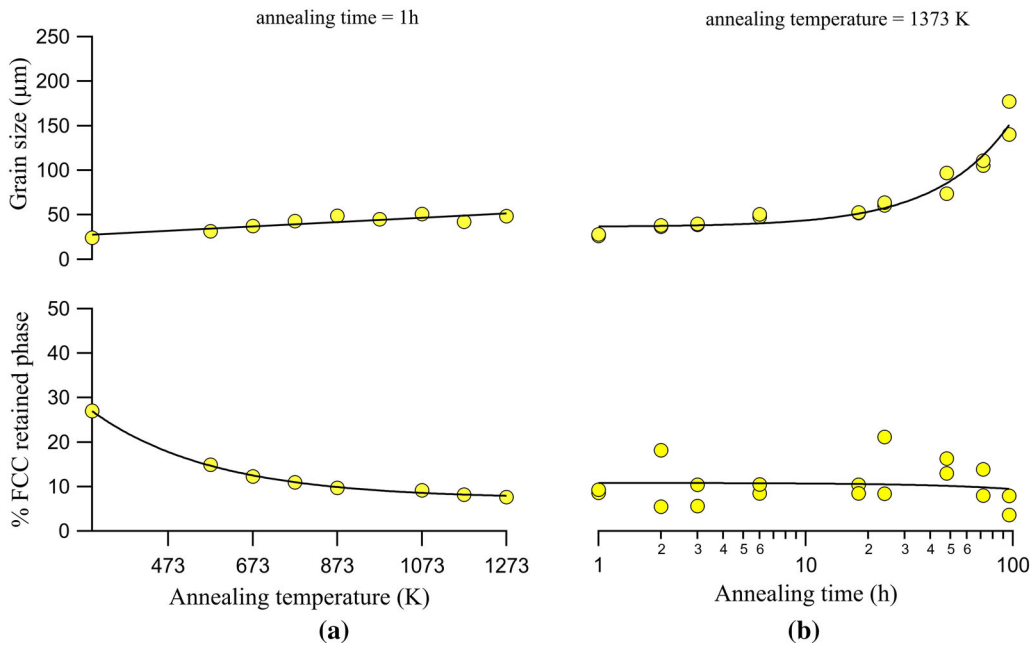


Fig. 6—Influence of annealing conditions [temperature for a time of 1 h (a) and time for a temperature of 1373 K (b)] on grain size and retained FCC phase proportion evolution.

the selected annealing temperature. These results were then compared with previous works for a 1373 K annealing temperature with durations ranging from 1 to 96 hour.^[27] The grain size, deduced from metallographic observations, slightly increases with annealing temperature but does not seem very significant compared to the power type increase appearing from 20 hour of heat treatment at 1373 K. Concerning the proportion of retained FCC phase, it exponentially decreases from 28 pct (as received) down to almost 10 pct for 873 K annealing, in accordance with Sanderson.^[7] For annealing temperatures > 873 K or longer annealing durations, this proportion remains constant.

Overall, these results allow explaining the final FCC phase proportion met after the thermal cycle. In fact, the thermal cycle applied during the previous *in situ* analysis included a heating stage until 773 K. This treatment induced a complete transformation of the HCP phase and significantly reduced the proportion of residual FCC phase at room temperature.

The results of Figure 6 clearly show that annealing treatments at moderate temperature ($T_{annealing} < T_{HCP-FCC}$) enable homogenization of the microstructure with a reduction of the retained FCC proportion combined with limited grain growth. The energy required for phase transformation is much lower than that for grain growth, showing to some extent the independence of these two phenomena.

The influence of the initial microstructure (*i.e.*, the retained FCC phase ratio and grain size to a lesser extent) on the phase transformation, performed using DSC, is plotted in Figure 7. Austenitic and martensitic transformation peaks are tracked during the DSC thermal cycle, on the as-received Co specimen as well as on the 573 K, 673 K and 773 K annealed samples

with 40 K/min cooling rate. The temperature of the HCP → FCC transformation increases with annealing temperature. The results show that the temperature to initially transform the HCP phase is directly related to the initial proportion of the retained FCC phase: the higher the annealing temperature, the lower the retained FCC volume fraction and the higher the HCP → FCC phase transformation temperature. Indeed, austenitic transformation needs more thermal energy to enable phase transformation as the HCP volume fraction to be transformed increases. In return, since the reverse transformation (*i.e.*, FCC → HCP) takes place during cooling with 100 pct FCC phase (austenitic transformation is completely finished at 773 K), the martensitic transformation temperature is then unchanged during cooling.

Despite a microstructure that appears to be stable, when subjected to thermal cycles around the transformation hysteresis (593 K to 773 K), the sample annealed at 773 K for 1 hour (see Figure 8) shows an austenitic temperature, which only becomes stable after about 15 cycles. It could be noted that the austenitization temperatures of the as-received sample and the two other annealed samples stabilize at the same value (≈ 721 K). This observation shows that it is necessary to transform the material about 15 times to homogenize it and to make its temperature $T_{HCP-FCC}$ independent of the following heat treatments. As displayed in Figure 8, the martensitic transformation temperature does not depend on the initial microstructure and therefore on annealing temperature. This fits to the fact that it transforms the same FCC phase proportion (*i.e.*, 100 pct). In the same way, this transformation is insensitive to the number of thermal cycles as the $T_{FCC-HCP}$ temperature varies < 2 K.

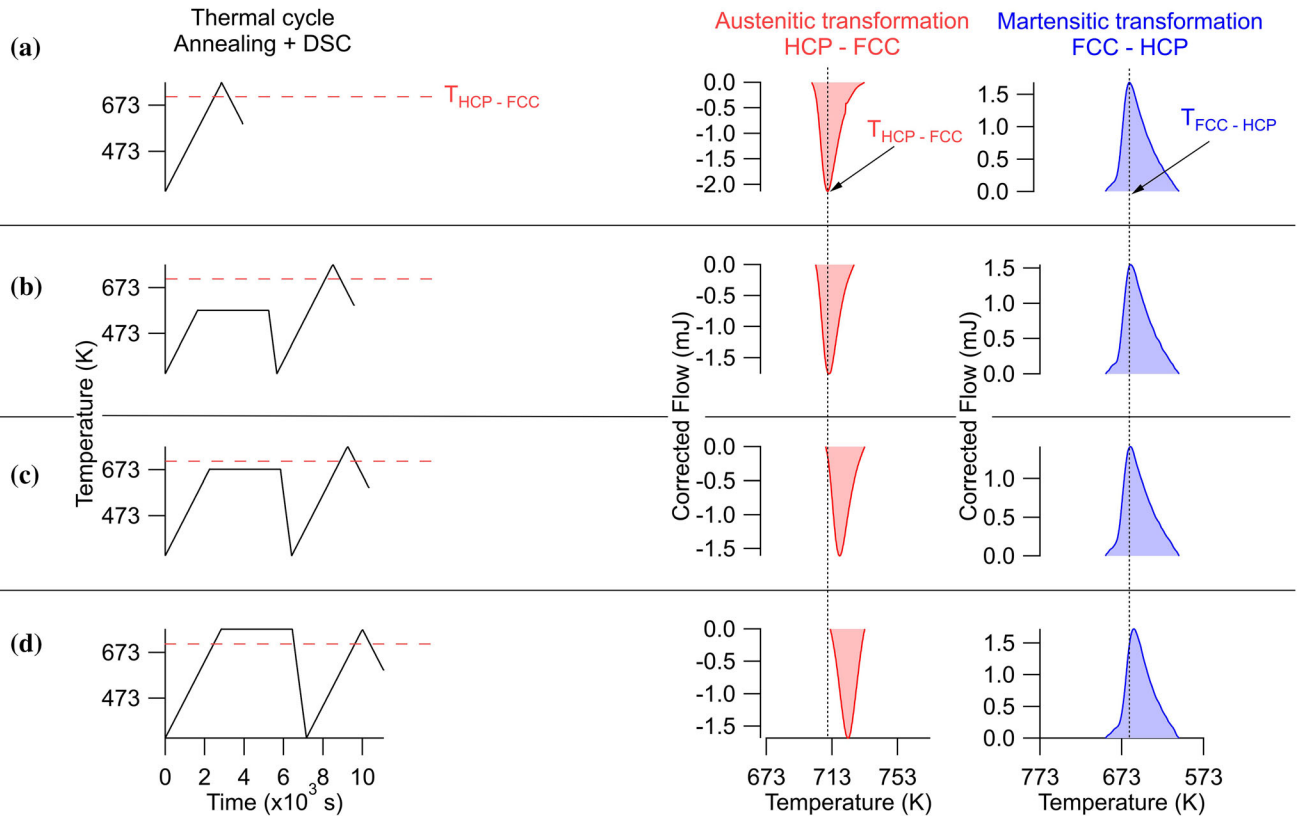


Fig. 7—Thermal loading paths in DSC performed for as-received (a), 573 K (b), 673 K (c) and 773 K (d) annealed samples with corresponding austenitic (red) and martensitic (blue) transformation peak tracking (Color figure online).

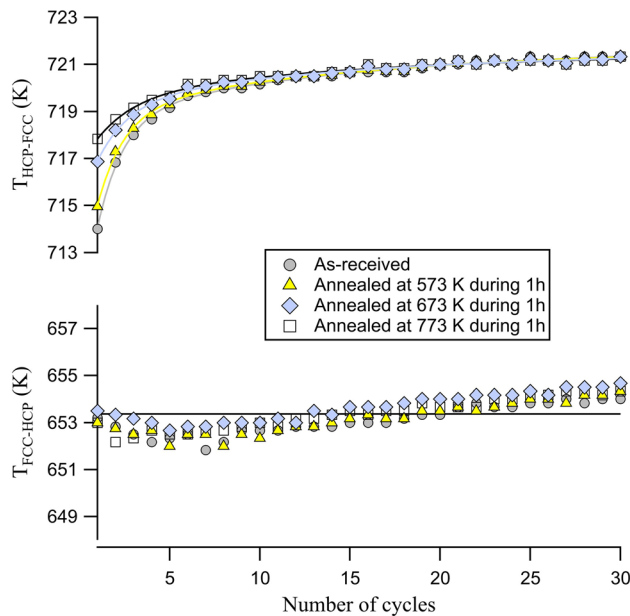


Fig. 8—Temperatures of HCP \rightarrow FCC and FCC \rightarrow HCP transformations as a function of the number of applied DSC cycles (up to 30 cycles) of the as-received sample superposed with the results of 573 K, 673 K and 773 K annealed samples.

Bauer *et al.*^[23] showed a grain growth of 15 to 80 μm with 60 DSC cycles, which does not influence the stabilized transformation temperature after 15 cycles.

An additional study was carried out on samples with different grain sizes and the same FCC proportion ($d = 100 \mu\text{m}$, $f_{\text{FCC}} = 0.1$ for an annealed sample during 48 hour at 1373 K and $d = 25 \mu\text{m}$, $f_{\text{FCC}} = 0.1$ for an annealed sample during 1 hour at 1373 K). The stabilized transformation temperature after 30 cycles is clearly independent of the initial grain size.

B. Allotropic transformation during mechanical deformation

1. Phase proportion evolution and work hardening during tensile test

The mechanical behavior in tension can be divided into three distinct stages. The first one is the elastic part. Zhou *et al.*^[28,29] have shown that this stage is characterized by a kinking nonlinear elasticity resulting in fully reversible hysteresis induced by nucleated dislocation loops in the slipping favored plane (the basal plane in the present case).

The second one, named stage A, characterizes the first work-hardening stage and appears from a strain of 0.0045 up to 0.018 (Figure 9). This stage is associated with a large reduction of the work-hardening rate and is controlled by planar and single glide of basal dislocations.^[9] However the combination of basal slip and volume change during transformation^[26] does not satisfy von Mises criterion, which requires five independent shear systems to undergo homogeneous strain without

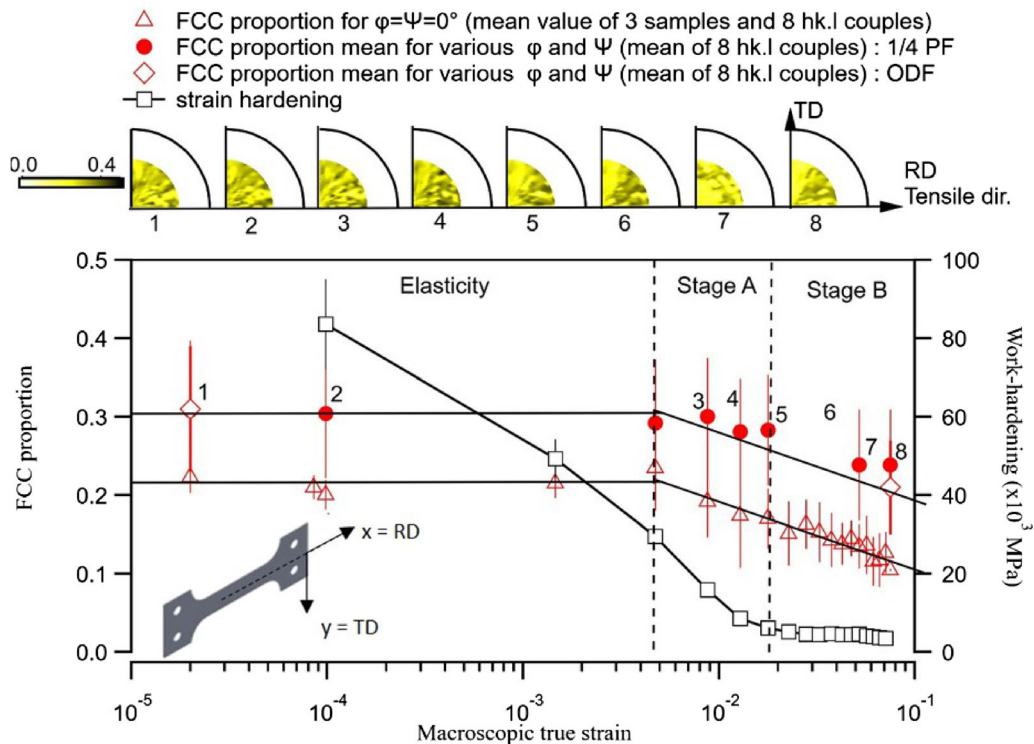


Fig. 9—FCC → HCP transformation evolution as macroscopic strain increases. Relationship between FCC phase proportion (red open triangle) and the deformation stages illustrated by work hardening (black open square). Monitoring of the phase transformation anisotropy for various (φ, ψ) orientations (maps) during tensile straining with the corresponding average values (red solid circle) (Color figure online).

changes in volume for a polycrystal. To accommodate the plastic deformation and since the FCC to HCP phase transformation is a low energy transformation requiring only simple shear, the formation of martensitic phase can be considered equivalent to the formation of twins.

Above a strain level of 0.018, the slope of the work-hardening rate is lowered to an almost constant value corresponding to stage B. This stage is described by twinning nucleation and growth. Martinez *et al.* have shown that compression $\{10.1\}_{\text{HCP}}$ and tensile $\{10.2\}_{\text{HCP}}$ twins are the main twinning modes representing respectively 16 pct and 66 pct of total observed twin planes.^[9]

Figure 9 highlights the effect of these deformation mechanisms on the allotropic transformation for a tensile sample strained along the rolling direction. The fast track FCC phase proportion, determined from θ - 2θ spectra achieved at $(\psi = 0 \text{ deg}, \varphi = 0 \text{ deg})$, is plotted (open triangles) versus the macroscopic applied true strain. This figure shows a transformation of the initial residual FCC phase into HCP phase initiated by plasticity. From the beginning of stage A to the end of stage B, this transformation is done gradually and linearly with the logarithm of the applied strain. To ensure the reliability and reproducibility of the experimental data, the tests were repeated three times by three different investigators. The FCC phase proportion evolution during tensile loading can be expressed by the following proposed straightforward equation:

$$\text{FCC proportion} = a * \log(\varepsilon) + b, \quad [4]$$

where the coefficients are $a = -0.089 \pm 0.006$ and $b = 0.017 \pm 0.01$, with a linear regression coefficient $R^2 = 0.93$. In comparison, Sanderson found $a = -0.1$ and $b = 0.019$ for polycrystalline samples with $10 \mu\text{m}$ grain size.^[6] The experimental slope is similar in stage A and stage B, leading to the conclusion that the phase transformation does not seem to be affected by the activation of twinning during stage B.

To take into account a doubtless evolution of the texture with the mechanical loading and to study the anisotropy of the phase transformation, the FCC phase proportion is determined for each of the (ψ, φ) couples covering a quarter of a pole figure ($0 \text{ deg} < \psi < 55 \text{ deg}$, $0 \text{ deg} < \varphi < 90 \text{ deg}$) using the eight-plane family couples detailed in Table I. Values are then averaged and results are plotted (red solid circles named $\frac{1}{4}$ PF) in Figure 9. Phase ratio evolution shows the same tendency as the one determined at $(\psi = 0 \text{ deg}, \varphi = 0 \text{ deg})$ for the two plasticity stages, with the same slope but a b -coefficient equal to 0.117 ± 0.007 . However, these averaged values are higher because of the influence of the texture on the quantitative determination of the phase proportion. Calculations of the phase proportion taking into account the ODF (red open lozenges in Figure 9) from the complete recalculated PFs were performed on the as-received material and on a specimen strained at 0.078 to confirm the relevance of the results obtained over a quarter of the experimental PF under loading.

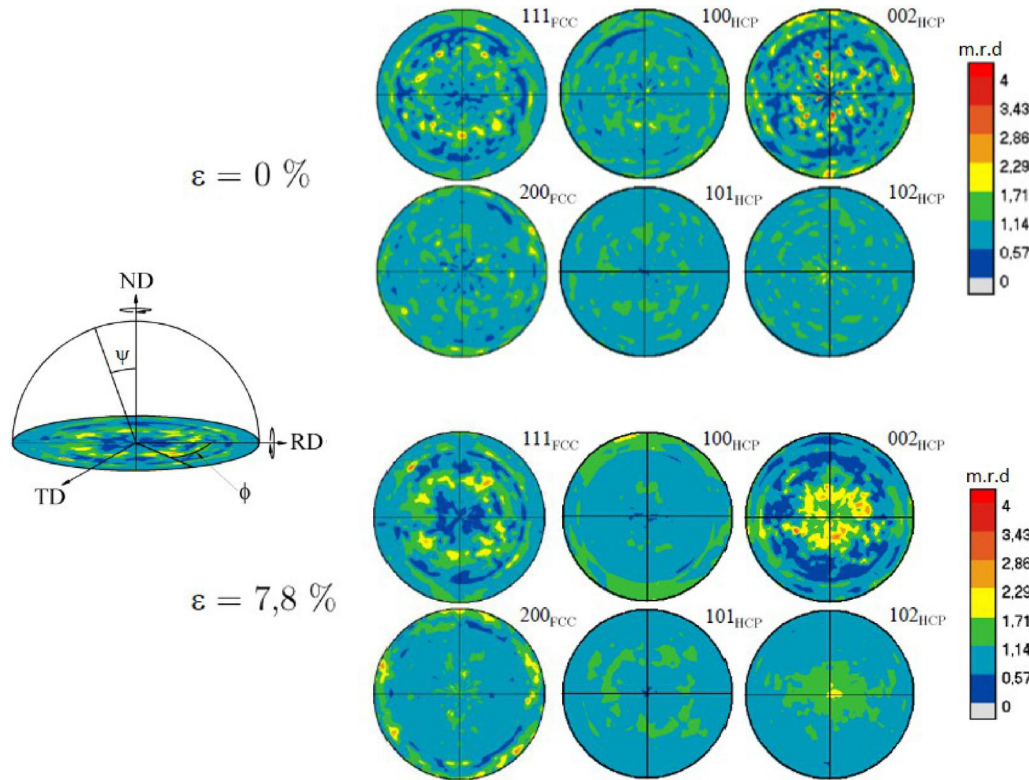


Fig. 10—Recalculated $\{10.0\}_{\text{HCP}}$, $\{00.2\}_{\text{HCP}}$, $\{10.1\}_{\text{HCP}}$, $\{10.2\}_{\text{HCP}}$, $\{111\}_{\text{FCC}}$ and $\{200\}_{\text{FCC}}$ PFs of the as-received sample and of a sample strained at 7.8 pct along the RD.

Table III. $\{00.2\}$ and $\{10.0\}$ PF Reorientations Peculiar to Twinning Systems and Phase Transformation According to the Three Studied Configurations

	Twinning System ^[32]	Twinning Shear ^[33–35]	ψ -Angle Reorientation on $\{00.2\}$ PF	ψ -Angle Reorientation on $\{10.0\}$ PF
(a) Tension twin $\sigma // c\text{-axis}$	$\{10.2\}\langle 10.1 \rangle$	0.13	5 deg	85 deg
(b) Compression twin $\sigma \perp c\text{-axis}$	$\{10.1\}\langle 10.2 \rangle$	0.14	56 deg	34 deg
(c) FCC-HCP transformation $\sigma // (10.2)$			43 deg ($\{111\}$) 66 deg ($\{111\}$)	

Regarding the experimental complexity to carry out ODF and since the texture does not fundamentally change the results, the choice was made to simplify the quantification of phase proportions at a single position (*i.e.*, $\psi = 0$ deg, $\phi = 0$ deg).

2. Crystallographic analysis of the strain-induced phase transformation and the deformation mechanisms

Deformation mechanisms and phase transformations can be explained by a crystallographic analysis, comparing the different texture components observed on the recalculated PFs obtained by XRD on a sample before and after straining. Figure 10 shows recalculated $\{10.0\}_{\text{HCP}}$, $\{00.2\}_{\text{HCP}}$, $\{10.1\}_{\text{HCP}}$, $\{10.2\}_{\text{HCP}}$, $\{111\}_{\text{FCC}}$ and $\{200\}_{\text{FCC}}$ PFs of the as-received sample and of a sample strained at 7.8 pct along the RD. Except for the habit plane between HCP and the retained FCC, it can

be assumed that the initial state of the HCP phase is not textured compared to the deformed state, which exhibits distinctive poles that can be seen on most PFs.^[30]

If the sample shows an isotropic orientation distribution in the initial state, three specific orientation cases of the HCP lattice with respect to the loading direction are assumed to be sufficient to study the orientation dependence of deformation mechanisms and phase transformation: *c-axis* parallel, normal or inclined with respect to the loading direction, as shown in Table III.

As described in the 3.2.1 subsection, the plastic behavior of high-purity polycrystalline cobalt exhibits two distinctive stages which correspond to the activity of basal slip (stage A) and twinning deformation modes (stage B). The determination of Schmid's factor of the basal plane for the three specific orientation cases [$\sigma // c\text{-axis}$ (a), $\sigma \perp c\text{-axis}$ (b) and $\sigma // (10.2)$ (c)] shows that the

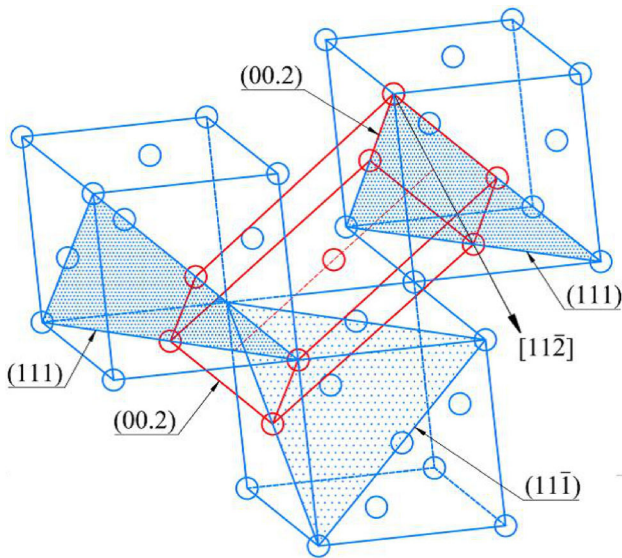


Fig. 11—Schematic representation of the orientation relationship between the FCC structure (in blue) and the HCP structure (in red) once shear has been achieved along the $[11\bar{2}]$ FCC direction.

unique configuration enabling such a slipping activity is (c): (10.2) plane parallel to the specimen surface with a Schmid's factor close to 0.5 (the most suitable configuration for basal slip). Configurations (a) and (b) will then be the most likely to show twin activity. Two types of twins have been frequently observed in deformed high-purity polycrystalline cobalt.^[9,33] The first one is the tensile twin $\{10.2\}\langle 10.1\rangle$, which activates when the HCP lattice undergoes a tensile strain along the c -axis because of the ratio $c/a < \sqrt{3}$.^[32] It represents 66 pct of the observed twinning modes in deformed cobalt and leads to a crystal rotation of 85 deg. The second is the compression twin $\{10.1\}\langle 10.2\rangle$, observed at a level of 16 pct and associated with a crystal rotation of 56 deg.

In addition to the deformation mechanisms, strained cobalt also presents a phase transformation FCC \rightarrow HCP, which is diffusionless and occurs by dislocation gliding on the habit plane $\{111\}/\{00.2\}$, causing shear along the $[11\bar{2}]_{\text{FCC}}$ direction (equivalent to the HCP direction $[11.0]$). The phase transformation is called multivariant because of its ability to occur on several $\{111\}_{\text{FCC}}$ planes, which display rotation angles of 70.53 deg between them^[12] (illustrated in Figure 11). However, due to the compactness difference between the two phases, the resulting rotational angle after the phase transformation FCC \rightarrow HCP becomes 71.4 deg according to the orientation relationship established by Shoji-Nishiyama.^[35] Hence, the resulting crystal undergoes a theoretical volume change of about -0.3 pct, which corresponds to a slight contraction along the c -axis.^[26,36] This phase transformation is more likely to be initiated when the habit plane $\{111\}/\{00.2\}$ shows an intermediary inclination regarding the loading direction^[13,14] corresponding to (c) the configuration in Table III. The crystallographic mechanism of FCC \rightarrow HCP phase transformation is illustrated in Figure 11, showing the FCC lattice atoms displacement along the $[11\bar{2}]$ direction and the formation of the HCP lattice from three $\{111\}$ FCC planes.

The crystallographic analysis carried out on the PFs of the deformed sample highlights the activated twin modes as well as the FCC \rightarrow HCP phase transformation induced by mechanical loading. It should be underlined that only two twin systems $\{10.2\}\langle 10.1\rangle$ for configuration (a) and $\{10.1\}\langle 10.2\rangle$ for configuration (b) were clearly identified using the PFs of the sample loaded up to 7.8 pct strain. Those actually match the lowest shear twinning values.^[32–34]

In the first configuration considered (a), the tensile twin mode $\{10.2\}\langle 10.1\rangle$ induces a crystal reorientation of 85 deg. This configuration concerns the reorientation of 85 deg of the c -axis, which was initially parallel to the loading direction (displayed by the orange solid line lattice projection in Figure 12(b) and became misaligned by 5 deg compared to the normal of the sheet plane (ND) (displayed by the orange dashed line lattice projection in Figure 12(b)). For the twinned part, it results in an angle of 85 deg between ND and the normal of the twinned prismatic plane (10.0) and an angle of 5 deg between ND and the normal of the twinned basal plane (00.2) . These crystallographic reorientations of the twinned region compared to the parent crystal are depicted by intensity reinforcement arcs on $\{00.2\}$ and $\{10.0\}$ PFs at 5 deg and 85 deg (identified by dashed orange rings in Figure 12(a), respectively). On the $\{10.0\}$ PF, the orientation reinforcement is preferably done at 90 deg from the loading direction in the sheet plane (TD).

In the second configuration considered (b), the compression twin mode $\{10.1\}\langle 10.2\rangle$ causes a crystal reorientation of 56 deg. Therefore, the resulting orientations of the twinned basal plane (00.2) and twinned prismatic plane (10.0) to the sample surface are 56 deg and 34 deg, respectively (displayed by pink dashed line lattice projection in Figure 12(b)). These crystallographic reorientations are highlighted by intensity reinforcement rings (dashed pink rings in Figure 12(a), which can be observed on $\{00.2\}$ and $\{10.0\}$ PFs at 56 deg and 34 deg, respectively).

In the third configuration considered (c), the FCC \rightarrow HCP phase transformation induced by tensile straining can be observed on $\{10.2\}$, $\{00.2\}$, $\{111\}$ and $\{200\}$ PFs (dashed black circle in Figures 12(a) and 13(a)). Because of the intermediate inclination of the HCP lattice, the (10.2) HCP plane is parallel to the sheet plane. Thus, the ND matches the central pole (at $\psi = 0$ deg) observed on the $\{10.2\}$ PF. As described above, the FCC \rightarrow HCP phase transformation is multivariant and may occur on several $\{111\}$ FCC planes. For this configuration and considering Shoji-Nishiyama's relationship, the habit plane $(111)/\{00.2\}$ is at an angle of 43.1 deg to the sample surface and the $(11\bar{1})$ one at an angle of 66 deg, as illustrated on the $\{00.2\}_{\text{HCP}}$ and $\{111\}_{\text{FCC}}$ PFs (dashed black circle in Figures 12(a) and 13(a)). Finally, the (200) FCC plane is oriented at 79 deg to the ND and depicted by an intensity reinforcement located at this ψ value on the $\{200\}_{\text{FCC}}$ PF.

Another way to analyze the evolution of the FCC \rightarrow HCP phase transformation with mechanical loading as well as the evolution of the main tensile twin

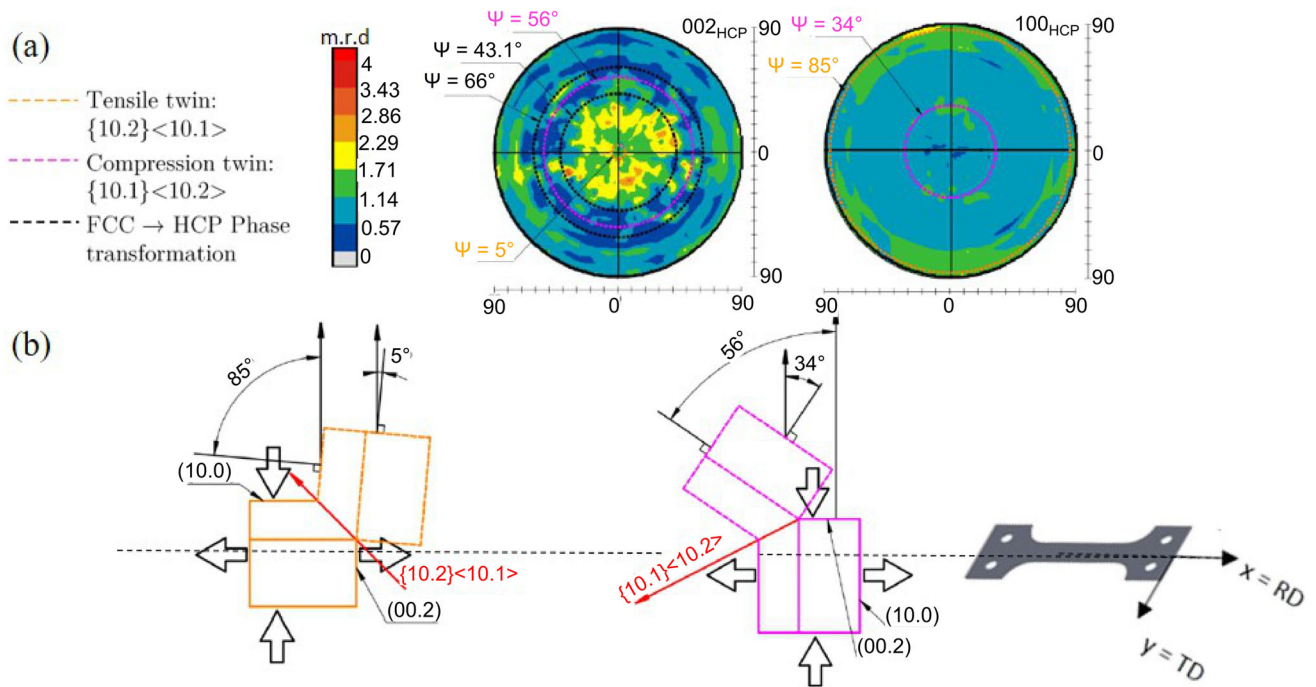


Fig. 12—Identification of the $\{10.2\}\langle 10.1 \rangle$ tensile twinning system, $\{10.1\}\langle 10.2 \rangle$ compression twinning system and phase transformation on $\{00.2\}$ and $\{10.0\}$ PFs for the sample loaded up to 7.8 pct strain (a). Schematic representation of reorientations caused by the two twin systems (b).

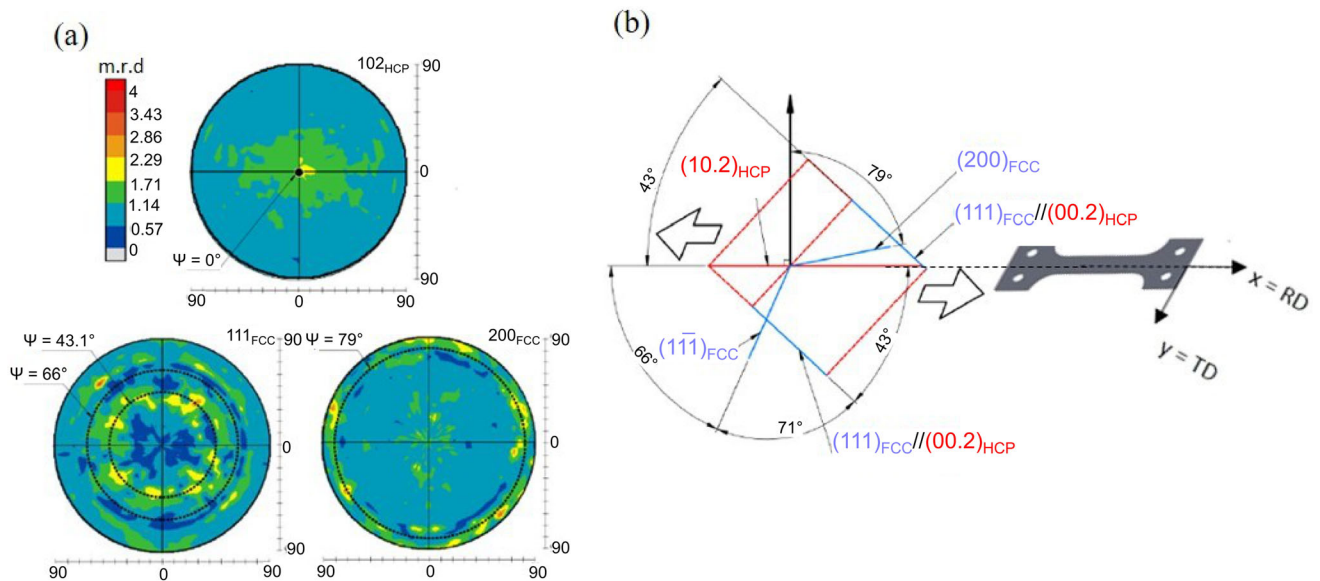


Fig. 13—Identification of the phase transformation from $\{10.2\}_{HCP}$, $\{111\}_{FCC}$ and $\{200\}_{FCC}$ PFs for the sample loaded up to 7.8 pct (a). Schematic representation of misorientations caused by the phase transformation (b).

deformation mode ($\{10.2\}\langle 10.1 \rangle$) is to follow the integrated intensities of the peaks reflecting these two phenomena. Figure 14 shows the tracking of the integrated intensities of $\{00.2\}$ and $\{10.2\}$ peaks during straining (for ψ respectively close to 5 deg and 0 deg) which correspond, respectively, to the activity of the twinning mode $\{10.2\}\langle 10.1 \rangle$ and the FCC \rightarrow HCP phase transformation. It can be seen that the integrated intensity of peak $\{00.2\}$ remains unchanged during

straining until the beginning of stage B for which plasticity is governed by twinning. Thereafter, the integrated intensity of the $\{00.2\}$ reflection linearly increases with the macroscopic strain. The monitoring of the integrated intensity of the $\{10.2\}$ peak shows that the phase transformation, initiated by basal slip, starts at the beginning of the plasticity, in agreement with the results obtained for the FCC volume fraction evolution (see Figure 9). Subsequently, the integrated intensity of

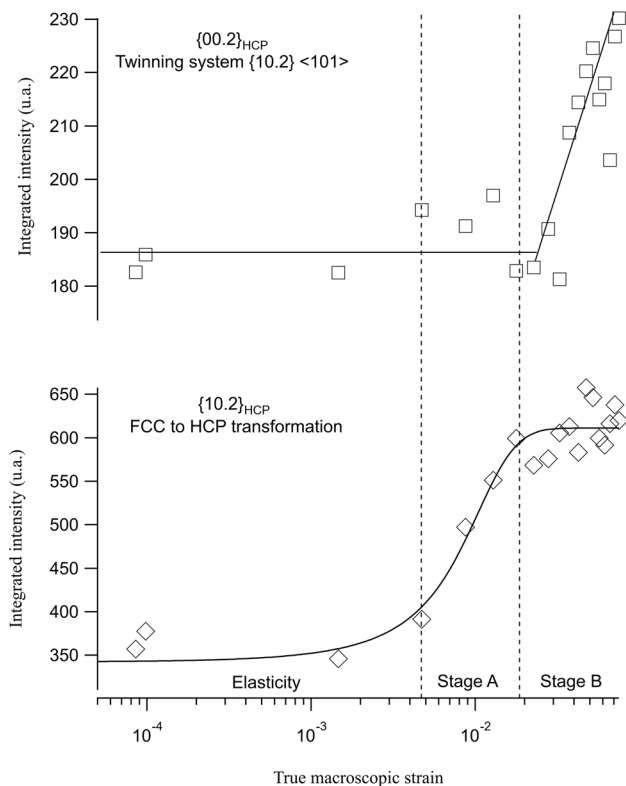


Fig. 14—Evolution of the integrated peak intensity at $\psi = 0$ deg for the $\{10.2\}$ reflection and around $\psi = 5$ deg for the $\{00.2\}$ reflection during a tensile test along the rolling direction.

the $\{10.2\}$ peak increases with macroscopic strain until the end of stage A. At this strain level, the twinning mechanism is activated and becomes the main deformation mode, which causes a lattice reorientation and a possible stress relaxation. Therefore, the slope of the integrated intensity evolution of $\{10.2\}$ reflection tends towards 0 and remains unchanged with increasing macroscopic strain. Thus, at stage B, the evolution of the integrated intensity of the $\{10.2\}$ reflection seems to show a competition between the phase transformation and the twinning process.

The monitoring of internal lattice strains (determined using Eq. [3]) of some $\{hkl\}$ plane families of HCP and FCC phases during tensile tests is illustrated in Figure 15. To compare these results with those obtained during the cooling of the thermal cycle (Section III-A-2), the internal lattice strains related to the two loading types (thermal and mechanical) are thus superimposed while adapting the temperature range of the thermal loading to the FCC \rightarrow HCP phase transformation window so that it suits stage A of the tensile test, for which only the FCC \rightarrow HCP phase transformation is occurring. As Figure 15 shows, this means that the slope of the macroscopic stress vs. lattice strain curves (in gray) during the tensile loading in stage A is similar to the slope of the curves temperature vs. lattice strains (in blue) obtained during cooling, except for the case of the $\{10.2\}$ reflection, which exhibits a higher slope in stage A. For a reminder, the $\{00.2\}$ basal slip is the only deformation mode in this stage. It comes along

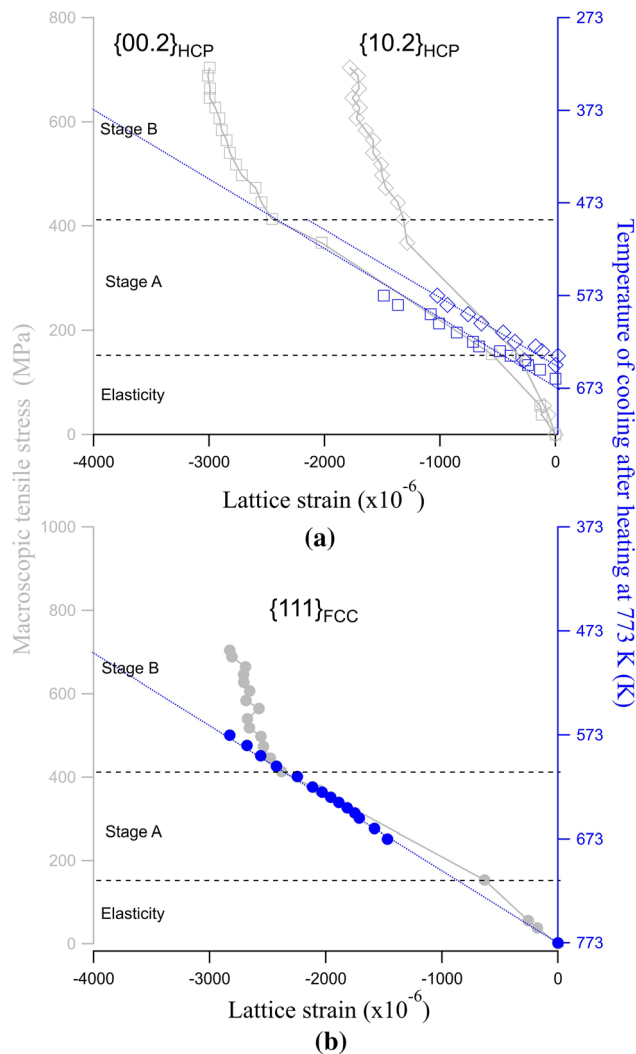


Fig. 15—Example of lattice strains for $\{00.2\}_{\text{HCP}}$ and $\{10.2\}_{\text{HCP}}$ (a) and $\{111\}_{\text{FCC}}$ (b) reflections during a tensile test along the rolling direction (gray symbol) with those measured during a cooling stage after a heating at 773 K (blue symbol) (Color figure online).

with a phase transformation, which occurs in a plane shared by the two FCC and HCP crystallographic structures (*i.e.*, the habit plane). From the beginning of stage B, a deviation from this linearity appears, leading to a lower evolution of the internal lattice strains with the macroscopic stress. The main deformation mode in stage B is twinning (mostly $\{10.2\}$ type), which induces reorientations of the crystal lattice. Thus, a stress relaxation can be generated within twinned grains and causes a lattice strain decrease. In this stage a competition between twinning and phase transformation can therefore be highlighted. The comparison between the internal lattice strain values at the beginning of stage B shows that the $\{10.2\}$ family plane deforms elastically less than the others before twinning. This result is consistent with the fact that, in the configuration (10.2) plane parallel to the sheet plane (c), the deformation can be accommodated by basal slip before that plasticity is controlled by twinning.

IV. CONCLUSIONS

In the present work, new experimental results refresh and reinforce the scarce and dated literature on the phase transformations and strengthening mechanisms of polycrystalline cobalt from the 1960s. The specific *in situ* temperature experiments showed that the FCC \leftrightarrow HCP phase transformation displays a temperature hysteresis between heating and cooling coupled to a macroscopic dilatometric hysteresis. However, the analysis of elastic lattice strains during the transformation does not exhibit this phenomenon. Complementary XRD studies of the phase transformation have highlighted the influence of the initial microstructure. In this work, a new and original *in situ* XRD study under mechanical loading was performed revealing that the martensitic transformation of the initial FCC residual phase can be induced by the plasticity and coupled with the strain-hardening mechanisms. FCC to HCP transformation is activated by basal slip during the work-hardening stage A and continues during stage B with a competition with the twin mode.

REFERENCES

1. G. Bouquet and B. Dubois: *Ser. Metall.*, 1978, vol. 12, pp. 1079–81.
2. A.E. Ray, S.R. Smith, and J.D. Scofield: *J. Phase Equilibria*, 1991, vol. 12, pp. 644–48.
3. G. Fleurier, E. Hug, M. Martinez, P.-A. Dubos, and C. Keller: *Philos. Mag. Lett.*, 2015, vol. 95, pp. 122–30.
4. H. Matsumoto: *J. Alloys Compd.*, 1995, vol. 223, pp. L1–L3.
5. H. Matsumoto: *Physica B*, 2003, vol. 334, pp. 112–17.
6. C.R. Houska, B.L. Averbach, and M. Cohen: *Acta Metall.*, 1960, vol. 8, pp. 81–87.
7. C.C. Sanderson: PhD Thesis, University of British Columbia, 1972.
8. V.M. Marx, C. Kirchlechner, B. Breibach, M.J. Cordill, D.M. Többens, T. Waitz, and G. Dehm: *Acta Mater.*, 2016, vol. 121, pp. 227–33.
9. M. Martinez, G. Fleurier, F. Chmelik, M. Knapek, B. Viguiet, and E. Hug: *Mater. Charact.*, 2017, vol. 134, pp. 76–83.
10. A. Seeger, H. Kronmüller, S. Mader, and H. Träuble: *Philos. Mag.*, 1960, vol. 6, pp. 639–55.
11. G. Fleurier, M. Martinez, P.A. Dubos, and E. Hug: *Mater. Sci. Forum.*, 2017, vol. 879, pp. 560–65.
12. J.W. Christian and W. Hume-Rothery: *Proc. R. Soc. Lond. Ser. Math. Phys. Sci.*, 1951, vol. 206, pp. 51–64.
13. H.T. Hesemann, P. Müllner, and E. Arzt: *Ser. Mater.*, 2001, vol. 44, pp. 25–30.
14. H.T. Hesemann, P. Müllner, O. Kraft, D. Nowak, S.P. Baker, K. Finkelstein, and E. Arzt: *Ser. Mater.*, 2003, vol. 48, pp. 1129–33.
15. H.-R. Wenk, S. Matthies, J. Donovan, and D. Chateigner: *J. Appl. Crystallogr.*, 1998, vol. 31, pp. 262–69.
16. N. Bruzy: PhD Thesis, Ecole Centrale de Nantes, 2018.
17. N. Bruzy, M. Coret, B. Huneau, G. Kermouche, M. Mondon, E. Bertrand, and L. Stainier: *Exp. Mech.*, 2019, vol. 59, pp. 1145–57.
18. W.A. Rachinger: *J. Sci. Instrum.*, 1948, vol. 25, pp. 254–55.
19. M.J. Buerger: *Proc. Natl. Acad. Sci. U.S.A.*, 1940, vol. 26, pp. 637–42.
20. J.T. Bonarski, M. Wróbel, and K. Pawlik: *Mater. Sci. Technol.*, 2000, vol. 16, pp. 657–62.
21. W. Betteridge: *Prog. Mater. Sci.*, 1980, vol. 24, pp. 51–142.
22. K. Lonsdale, C.H. MacGillavry, and G.D. Rieck: *International Tables for X-Ray Crystallography*, Kynoch Press, 1962, vol. 3.
23. R. Bauer, E.A. Jaegle, W. Baumann, and E.J. Mittemeijer: *Philos. Mag.*, 2010, vol. 91, pp. 437–57.
24. D. Gloaguen, B. Girault, B. Courant, P.-A. Dubos, M.-J. Moya, F. Edy, J. Rebelo Kornmeier: *Metall. Mater. Trans. A.*, 2020, vol. 51, pp. 951–61.
25. H. Bibring and F. Sebilliau: *Rev. Métallurgie.*, 1955, vol. 52, pp. 569–78.
26. G.W. Greenwood and R.H. Johnson: *Proc. R. Soc. Lond. Ser. Math. Phys. Sci.*, 1965, vol. 283, pp. 403–22.
27. G. Fleurier: PhD Thesis, Université de Caen, 2016.
28. A. Zhou: PhD Thesis, Drexel University, 2008.
29. A.G. Zhou, D. Brown, S. Vogel, O. Yehekel, and M.W. Barsoum: *Mater. Sci. Eng. A.*, 2010, vol. 527, pp. 4664–73.
30. Y.N. Wang and J.C. Huang: *Mater. Chem. Phys.*, 2003, vol. 81, pp. 11–26.
31. J.W. Christian and S. Mahajan: *Prog. Mater. Sci.*, 1995, vol. 39, pp. 1–157.
32. M.H. Yoo: *Metall. Trans. A.*, 1981, vol. 12, pp. 409–18.
33. M. Martinez and E. Hug: *Materialia*, 2019, vol. 7, p. 100420.
34. S. Vaidya, S. Mahajan, and C.M. Preece: *Metall. Trans. A.*, 1980, vol. 11, pp. 1139–50.
35. Z. Nishiyama: *Martensitic Transformation*, 1st ed., Academic Press, 1978.
36. F. Sebilliau and H. Bibring: *Inst. Met. Monogr.*, 1956, vol. 18, pp. 209–17.

Publisher's Note Springer Nature remains neutral with regard to jurisdictional claims in published maps and institutional affiliations.